

"This document is the Accepted Manuscript version of a Published Work that appeared in final form in iScience, Copyright © 2020 Elsevier Inc. after peer review and technical editing by the publisher. To access the final edited and published work see:

<https://www.sciencedirect.com/science/article/pii/S2589004220305666>

Analysis of the active species responsible for water oxidation using a pentanuclear Fe complex

Primavera Pelosin,¹ Marcos Gil-Sepulcre,¹ Pablo Garrido-Barros,¹ Dooshaye Moonshiram,² Jordi Benet-Buchholz¹, Carolina Gimbert-Suriñach¹ and Antoni Llobet^{*,1,3}

¹Institute of Chemical Research of Catalonia (ICIQ), The Barcelona Institute of Science and Technology (BIST), Avinguda Països Catalans 16, 43007 Tarragona, Spain.

²Instituto Madrileño de Estudios Avanzados en Nanociencia (IMDEA-Nanociencia), Calle Faraday 9, 28049 Madrid, Spain.

³Departament de Química, Universitat Autònoma de Barcelona, 08193 Cerdanyola del Valles, Barcelona, Spain.

*Corresponding author and Lead contact: Antoni Llobet, allobet@iciq.cat.

Summary

Water splitting with sunlight is today one of the most promising strategies that can be used to start the imperatively needed transition from fossil to solar fuels. To achieve this, one of the key reactions that need to be mastered is the electrocatalytic oxidation of water to dioxygen. Great developments have been achieved using transition metal complexes mainly based on Ru, but for technological applications it is highly desirable to be able to use earth abundant transition metals. The intrinsic chemistry of first row transition metals and in particular the lability of their M-L bonds in water imposes serious challenges for the latter to work as real molecular catalysts. The present work addresses this issue based on a molecular pentanuclear Fe₅ complex and describes the different protocols and tests that need to be carried out in order to identify the real active species, responsible for the generation of dioxygen.

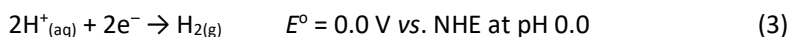
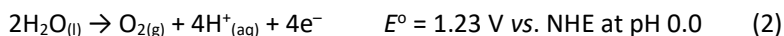
Keywords

Water oxidation catalysis, first row transition metals, redox properties, solar fuels.

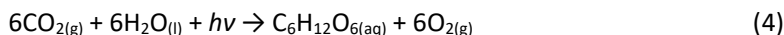
Introduction

One of the main threats on today's lifestyle of our modern societies is the increased global warming effect caused through the emission of greenhouse gases. The massive burning of fossil fuels over the course of the past decades has resulted in an alarming increase in carbon dioxide concentrations responsible for the global climate change and concomitant environmental issues.

It is thus extremely urgent to replace fossil fuels by new energy conversion schemes based on clean and environmentally respectful fuels. A potential option is the production of H₂ through water splitting with sunlight (hv-WS) as indicated in equation 1.



Hydrogen generated in this manner is termed solar fuel. Further hv-WS is also termed as artificial photosynthesis (Grätzel, 1981; Berardi *et al.*, 2014; Lewis, 2016; Nocera, 2017; Roger, Shipman and Symes, 2017; Guan *et al.*, 2018) because there are a number of analogies with this reaction and the one that occurs in the natural photosynthesis summarized in equation 4. (Nelson and Ben-Shem, 2004; McEvoy and Brudvig, 2006; Croce and Van Amerongen, 2014).



From a chemical perspective these analogies include:

a) both reactions are thermodynamically uphill, driven by sunlight and require the participation of light harvesting agents that can transfer the sun's energy into high energy density chemicals such as carbohydrates or H₂.; b) both processes need catalysts to speed up the redox reactions and c) the water oxidation reaction occurs in an identical fashion in natural photosynthesis and in hv-WS. In the former case a tetramanganese cluster located in photosystem II (PSII) is employed as a catalyst to speed up the water to dioxygen reaction.

The water oxidation reaction has long been regarded as a major bottleneck that ought to be solved to be able to develop devices based on hv-WS. However, during the last decade, a large degree of knowledge has been generated based on both oxide materials (Smith *et al.*, 2013; McCrory *et al.*,

2015; Godwin *et al.*, 2018) and molecular transition metal complexes (Blakemore, Crabtree, and Brudvig, 2015; Garrido-Barros *et al.*, 2017; Matheu *et al.*, 2019a; Matheu *et al.*, 2019b).

In this context, the molecular water oxidation catalysis field has experienced a significant progress over the last ten years powered by the promise of generating sustainable carbon neutral fuels based on water splitting (Lewis and Nocera, 2006, 2007; Llobet and Meyer, 2011). A particularly noteworthy contribution has been the development of water oxidation catalysts containing molecular Ru complexes due to the high degree of understanding of their performance at a molecular level. This has been achieved thanks to a thorough description of their reactivity, electrochemical and spectroscopic properties as well as a detailed characterization of their reaction intermediates, all combined with complementary computational models (Ellis *et al.*, 2010; Radaram *et al.*, 2011; Sala *et al.*, 2014; Matheu *et al.*, 2015; Keidel *et al.*, 2017).

It would be very convenient to use non-toxic earth abundant transition metal complexes such as Fe-based catalysts as WOCs for the generation of technologically useful devices. Few Fe-based WOCs have been reported so far but most of them are unfortunately not free from controversy since in most of the cases the real active catalytic species is most likely the corresponding oxide rather than the initial molecular complex (Hoffert *et al.*, 2013; Pattanayak *et al.*, 2017). Therefore, rigorous analysis of the active species is essential in order to achieve meaningful information of the catalytic species, not only in water oxidation but in the field of molecular electrocatalysis (Kaeffer *et al.*, 2016; Folkman *et al.*, 2018).

The present work analyzes the water oxidation catalysis initially associated to the complex $[\text{Fe}^{\text{II}}_4\text{Fe}^{\text{III}}(\mu_3\text{-O})(\mu\text{-bpp})_6]^{3+}$, from now on labeled as $[\text{Fe}^{\text{II}}_4\text{Fe}^{\text{III}}]^{3+}$ or Fe_5^{3+} , (Okamura *et al.*, 2016) where bpp^- is the anionic tetradentate dinucleating bridging ligand 3,5-bis(2-pyridyl)pyrazolato, see Figure 1 for a drawing of its two electron oxidized derivative. The transformation of the metal complex into the corresponding oxides is a major concern here since it precludes the correlation of reactivity with the catalytic process and thus becomes a futile exercise. **Such exercises could generate misleading information in the water oxidation field.**

This manuscript summarizes the main critical tests that need to be carried out to prove the molecular nature of the catalytic processes using Fe_5^{3+} but that it obviously can be extended to other iron complexes as well as to other earth-abundant first row transition metal complexes.

Results

1. Fe₅ⁿ⁺ synthesis, structure and redox electronic properties in MeCN

The reaction of Fe(SO₄)·7H₂O and bpp⁻ in MeOH in an open atmosphere gives rise to the formation of a pentanuclear complex [Fe^{II}₄Fe^{III}(μ₃-O)(μ-bpp)₆]³⁺, [Fe^{II}₄Fe^{III}]³⁺ or Fe₅³⁺, with relatively high isolated yield of ~ 72 %. Although UV-vis spectroscopy shows that the reactions proceed quantitatively (see Figure S3 in the SI), the decrease in the isolated yield is due to the crystallization process and the follow up operations needed to isolate a pure solid.

Complex Fe₅³⁺, can be cleanly and successively oxidized by 2 one-electron processes in MeCN reaching the high oxidation state complex [Fe^{II}₂Fe^{III}₃(μ₃-O)(μ-bpp)₆]⁵⁺, [Fe^{II}₂Fe^{III}₃]⁵⁺ or Fe₅⁵⁺, whose crystal structure is shown in Figure 1. In the structure, the metal centers are situated at the vertex of a triangular bipyramid where the bpp⁻ acts as bridging ligand between the axial and equatorial Fe whereas the oxido group bridges the three Fe sites situated in the equatorial plane. The axial Fe sites are hexacoordinated (CN₆) with a distorted O_h symmetry whereas the equatorial ones are pentacoordinated (CN₅) with a distorted C_{2v} symmetry. This crystal structure is very similar to the previously reported one for Fe₅³⁺ complex (Okamura *et al.*, 2016), except for a slightly shorter Fe-O and Fe-N distances as expected (Figure S1 and Table S1) (Sreerama and Pal, 2004).

Figure 1.

It is important to realize here that the quantitative yield of this reaction implies that the pentanuclear structure is especially stable from a thermodynamic perspective given the large number of complexes that can be potentially formed by mixing the bpp⁻ ligand and the iron [Fe^{II}(H₂O)₆]²⁺, (obtained from the dissolution of iron sulfate in water) as shown in Figure S2. These potential complexes range from simple mononuclear complexes with different number of bpp⁻ ligands bonded to the Fe center, to dinuclear, polynuclear etc. again with different numbers of coordinated bpp⁻ ligands attached to Fe. The formation of Fe₅³⁺ as the only complex generated in this reaction points to a scenario whereby the Fe-N bond is forming and breaking easily in agreement with the lability of high spin Fe(II) and Fe(III) complexes (Helm and Merbach, 2006). This is exemplified in Figure S2 where it shows the first Fe complexes that will most likely be made upon mixing Fe(II) and bpp⁻. The *fac*-[Fe(L)₃]⁻ complex will end up acting as a capping group for the final Fe₅³⁺ complex. Only the [Fe(L)(H₂O)₄]⁺ and the *cis,cis*-[Fe(L)₂(H₂O)₂] complexes will have the proper ligand geometrical coordination so that they can lead to the formation of *fac*-[Fe(L)₃]⁻ without the need of additional ligand rearrangements. All the other complexes will need to rearrange and thus Fe-N bonds will have to be broken and made anew to be able to lead to *fac*-[Fe(HL)₃]⁻. Thus, all the

potential complexes generated at the initial stages of the synthesis will reorganize in order to converge to the most thermodynamically stable complex which is, in this case, Fe_5^{3+} . A parallel phenomenon also occurs with other metal complexes such as Mn that can achieve a similar structural arrangement with bpp^- , such as $[\text{Mn}^{\text{II}}_4\text{Mn}^{\text{III}}(\mu\text{-bpp})_6(\mu_3\text{-O})]^{3+}$, Mn_5^{3+} , and also with related linearly arranged tetranucleating ligands (Bao *et al.*, 2010; Romain *et al.*, 2011).

While the Fe_5^{3+} is relatively stable in solution at low concentrations of water, the corresponding Mn analogue, the Mn_5^{3+} , decomposes almost immediately to generate the free ligand and $[\text{Mn}(\text{H}_2\text{O})_6]^{2+/3+}$ (Romain *et al.*, 2011). This indicates the capacity of H_2O to compete for the first coordination sphere of the Mn center, so that once a water molecule coordinates to a Mn center the whole structure collapses losing the stability provided by the pentanuclear arrangement.

In MeCN as solvent, the Fe_5^{n+} complex is a very rich molecule from a redox perspective accessing 6 different oxidation states ranging from $[\text{Fe}^{\text{II}}_5(\mu_3\text{-O})(\mu\text{-bpp})_6]^{2+}$, Fe_5^{2+} , where all the iron centers have oxidation state II up to $[\text{Fe}^{\text{III}}_5(\mu_3\text{-O})(\mu\text{-bpp})_6]^{7+}$, Fe_5^{7+} , where now all Fe centers have oxidation state III. All the oxidation states can be accessed by successive one electron electrochemically quasireversible processes, as can be observed in the CV in Figure 2 and in agreement with a previous report (Gouré *et al.*, 2016) (see SI Figure S4 and Table S2 for further details). All CV in this work are carried out using a glassy carbon (GC) electrode as a working electrode, a Ag^+/Ag (0.01 M) as reference and a Pt disk as auxiliary electrode unless explicitly mentioned. All potentials in this work are reported vs. Fc^+/Fc . The fully reduced species Fe_5^{2+} is air sensitive and thus needs to be isolated in an inert atmosphere. The fully oxidized species Fe_5^{7+} , displays a chemically reversible behavior during the CV time scale but on bulk electrolysis timescales is not stable and decomposes, indicating the high reactivity of such a high oxidation state species. All other Fe_5^{n+} species in intermediate oxidation states are stable and can be isolated as solids in an open air atmosphere that is in accordance with a previous report (Gouré *et al.*, 2016).

The electronic structure of the six Fe_5^{n+} ($n = 2-7$) complexes at the different oxidation states has been unambiguously established based on EPR and magnetic measurements (Gouré *et al.*, 2016). The six coordinated apical Fe(II) centers in Fe_5^{3+} have a low spin (LS) d^6 configuration whereas two equatorial Fe(II) have a high spin (HS) d^6 and the third equatorial Fe(III) is a low spin d^5 . On the other hand, for the highest oxidation state complex, Fe_5^{7+} , the apical Fe centers are LS whereas the equatorial ones are HS.

Figure 2.

2. Redox Properties in aqueous MeCN

2.1 The impact of $[H_2O]$ in the catalytic activity

In water, the Fe_5^{3+} complex is not soluble but it can be solubilized in mixtures of MeCN and H_2O . The latter is important since in the absence of water, the potential active species needed to enter into the water oxidation catalytic cycle cannot be formed. The electrochemical work reported here is carried out in mixtures of a MeCN solution containing 0.1 M tetraethyl ammonium perchlorate (TEAP) and water in a maximum 10:1 MeCN: H_2O volume ratio. This from now on will be referred in an abbreviated manner as 10:1 MeCN: H_2O .

In 10:1 MeCN: H_2O as solvent mixture the CV of Fe_5^{n+} is similar to the one reported in 0.1 M TEAP MeCN with a slight cathodic shift of roughly 40 mV for the wave associated with the $[Fe^II Fe^III_4]^{6+}/[Fe^II_2 Fe^III_3]^{5+}$ couple as can be observed in Figure 2. Further a large electrocatalytic current starting at 0.85 V is observed that is assigned to the oxidation of water to dioxygen. This electrocatalytic wave was wrongly assigned to the catalytic activity of a molecular Fe_5^{n+} complex (Okamura *et al.*, 2016). It was proposed based on DFT, that once the $[Fe^III_5]^{7+}$ species is reached, a solvent water molecule could coordinate in one of the equatorial iron centers forming $[Fe^III_5(H_2O)(\mu_3-O)(\mu-bpp)_6]^{7+}$, with increasing coordination number from CN_5 to CN_6 . A series of oxidations and an additional water coordination to a neighboring Fe center was then proposed to occur so that a sufficiently reactive species would form an O-O bond that might finally release dioxygen. The transition state energy for the initial step, the coordination of water and the formation $[Fe^III_5(H_2O)(\mu_3-O)(\mu-bpp)_6]^{7+}$, is highly endergonic by 18.9 kcal/mol and is proposed to be the rate determining step (rds) of this catalytic cycle (Liao, Masaoka and Siegbahn, 2018). This is in agreement with the high stability of the Fe_5^{n+} structure and thus the large energy needed to disrupt it. On the other hand, it also points out that once a water molecule coordinates a metal center, the whole structure might collapse with the formation of multiple Fe complexes containing different ratios of aqua and bpp^- bonded ligands. If this disruption occurs in close proximity with a glassy carbon electrode the new species will generate FeOx as will be shown below.

Figure 3 left shows the third CV cycle of Fe_5^{3+} within the potential range of -1.08 till 1.19 V at a scan rate of 10 mV/s in 10:1 MeCN: H_2O solution (the first cycle is reported in the SI in Figure S5A). While the waves associated with the Fe_5^{n+} molecular complex remain the same as in the first cycle (See Figure 2) the catalytic current in the third cycle increases nearly 5 times from approx. 200 $\mu A/cm^2$ up to approx. 1.0 mA/cm^2 at 1.19 V. This unambiguously indicates the formation of new catalytically active species potentially adsorbed at the surface of the electrode. Indeed, transferring the glassy

carbon electrode obtained after the CV into a clean electrolyte solution and scanning from 0.92 V till 1.19 V, shows a current density at 1.19 V that is close to 90% of the previous one. Further no redox waves associated with molecular $\text{Fe}_5^{\text{n}+}$ complex can be observed when scanning within the -1.08 till 1.19 V potential range (see Figure 3 left). These two experiments point out that FeOx are the main species responsible for the electrocatalytic activity observed here, given its well known catalytic behavior (Le Formal *et al.*, 2015). Further XAS spectroscopy was also carried on glassy carbon plates that gives additional support to the formation of FeOx adsorbed at the electrode surface as will be discussed a later on.

Figure 3.

A series of related experiments were also carried out by changing the relative concentration of H_2O from 1 till 10% in MeCN and are reported in the Figure S5B. In Figure 3 right a plot of the current density at 1.19 V versus the concentration of water is displayed for the initial Fe_5^{3+} solution and for the electrode obtained from this solution placed subsequently in a clean electrolyte solution. The very close values obtained here further point out that the $\text{Fe}_5^{\text{n}+}$ species are a precursor for the generation of FeOx that is actually the active catalyst. The difference between the initial current density and the one obtained in a clean electrolyte solution can be due to ligand oxidation, the formation of transient active species generated during the decomposition process to FeOx, or from the partial solubilization of the FeOx from the electrode.

As can be seen in Figure 3 right, the intensity of the wave at 1.19 V increases with the concentration of water thus clearly establishing a direct correlation between the H_2O concentration and the catalytic activity. This points out to the presence of a series of equilibria between the initial $\text{Fe}_5^{\text{n}+}$ complex and FeOx as depicted in Figure 4. The larger the concentration of water, the larger is the equilibrium shift towards the aquated species, and thus a larger amount of FeOx will be deposited at the surface of the glassy carbon electrode. Further, the increase in water concentration implies an increase in substrate concentration that can lead to a higher catalytic current.

Figure 4.

2.2 The influence of pH on the stability of the Fe_5^{n+} complex.

The stability of Fe complexes is strongly dependent on pH as has been shown in a number of occasions for related ligands (Draksharapu *et al.*, 2012; Hong *et al.*, 2013). The main driving force for decomposition process is the lability of the bonded ligands that can be substituted by solvent water ligands. In acidic pH this substitution process will be further enhanced by the protonation of the bonded ligands that will be strongly dependent on pH. In this respect, the pK_a of pyridinium ion is 5.5 and that of pyrazole is 14.2. However, when the Hbpp is coordinated to a transition metal as in the case of $[Ru(trpy)(Hbpp)]^{2+}$ (where trpy is 2,2':6',2''-terpyridine), then the pK_a of the pyrazole moiety becomes more acidic with pK_a values in the range of 5-7 depending on the oxidation state of the metal (Sens *et al.*, 2003). In basic pH, the anionic OH^- ligand will be responsible for the substitution process and subsequent generation of FeOx (Chen *et al.*, 2013; Hong *et al.*, 2013).

For water oxidation catalysis, the fact that every oxygen molecule evolved generates 4 protons implies that the local pH will also be strongly reduced in the double layer during water oxidation electrocatalysis. This will in turn strongly effect the stability of the complex leading to decomposition reactions at low local pHs. For this reason, it is extremely important to carry out water oxidation catalysis in the presence of a buffer so that the pH can remain practically constant. This strong influence of pH into the electrocatalytic activity is clearly manifested by observing the current density in the CV at 1.19 V for Fe_5^{3+} in the presence and absence of buffer (see Figure S6 right). Indeed, in the absence of a buffer, the current density observed is 44% larger than the one in the presence of a non-coordinating borate buffer that clearly suggests the influence of the local pH on the equilibria proposed in Figure 4.

CV experiments were also carried out at different pH values and it was found that from pH = 2-7, the behavior of the Fe_5^{n+} complex is basically the same (Okamura *et al.*, 2016). However below pH 2 the Fe_5^{3+} complex is not stable and decomposes to $[Fe^{II}(H_2O)_6]^{2+}$ and free ligand as is the case of related complexes reported in the literature (Draksharapu *et al.*, 2012; Hong *et al.*, 2013). Further, no electrocatalytic activity is observed at pH values below 2. (see SI Figure S7 for further details).

2.3 The formation of FeOx films at the surface of the GC electrode.

The nature of the FeOx deposited at the surface of the GC electrode was evaluated by means of electrochemical, spectroscopic and microscopy techniques. Figure 5 left, shows the results of 100 repetitive CVs scans from -0.44 till 1.19 V for a 0.2 mM solution of Fe_5^{3+} in a 10:1 MeCN:H₂O solution using a GC disk as a working electrode (GC). As it can be observed after the 100th cycle, the CV becomes nearly featureless with an increased double layer capacitance indicating that the initial

electrode has lost its conductivity. A simply eye inspection of the electrode shows the formation of a film at the surface. Placing this electrode into a clean solution containing a ferrocene solution 0.2 mM shows that the anodic III/II wave has lost 93.3% (see SI Figure S8) of its area with regard to a pristine electrode in exactly the same conditions, confirming the isolating nature of the oxide deposited at the electrode.

Figure 5.

The Scanning Electron Microscopy (SEM) image of this electrode does not show any boundary or particle shapes, but rather a homogeneous surface with similar morphology as the GC electrode, and thus we attribute this to the formation of a film. The nature of this film was further evaluated based on Energy-Dispersive X-Ray (EDX) Spectroscopy, Scanning Electron Microscopy (SEM) and X-ray photoelectron spectroscopy (XPS) displayed in the SI (Figure S9 and S11 top respectively). XANES (X-ray absorption near edge structure) and EXAFS (Extended X-ray absorption fine structure analysis) were also carried out on the $\text{Fe}_5^{\text{n}+}$ complex before (Figure S19-S21, Table S3) and after bulk catalysis (Figure 6) in a glassy carbon plate following exactly the same protocol used for the CV with the GC electrode. The XANES and EXAFS spectra shown in Figure 6 unequivocally show the spectral features of FeOx (Kuzmin and Chaboy, 2014; Tangwatanakul, 2017) at the electrode after the 100th cycle, thus discarding the potential surface absorption of the molecular $\text{Fe}_5^{\text{n}+}$ species. As observed by the red arrows in Figure 6B, a prominent increase in the amplitudes of the EXAFS peaks at apparent distances ~ 1.5 and 2.5 \AA are indeed observed in agreement with the EXAFS spectral features of Fe_2O_3 (shown in cyan).

Figure 6.

A closer inspection at the repetitive CV experiment provides additional insight into the progressive formation of the FeOx film. Figure 5 right shows a plot of the current density obtained at 1.19 V vs. $i_{p,a}$ of the $[\text{Fe}^{\text{II}}\text{Fe}^{\text{III}}_4]^{6+}/[\text{Fe}^{\text{II}}_2\text{Fe}^{\text{III}}_3]^{5+}$ redox wave preceding the electrocatalytic current. During the first ten cycles, the electrocatalytic current at 1.19 V increases its intensity whereas the $i_{p,a}$ of the $[\text{Fe}^{\text{II}}\text{Fe}^{\text{III}}_4]^{6+}/[\text{Fe}^{\text{II}}_2\text{Fe}^{\text{III}}_3]^{5+}$ wave decreases. This implies that the catalytic activity increases initially as active FeOx is being formed and deposited at the GC electrode. At the same time and due to the formation of non-conductive FeOx (potentially due to a thicker layer or different morphology), the available conductive surface area decreases and thus the intensity of the molecular $\text{Fe}_5^{\text{n+}}$ waves decrease as well. The next 20 cycles show a decrease of both currents due the non-conductive nature of the film generated at the electrode. From 50 to 100 cycles, small amounts of isolating FeOx are further deposited that generates a large increase of the capacitance at the electrode.

2.4 The formation of FeOx nanoparticles at the surface of the GC electrode.

The performance of the Fe_5^{3+} complex was evaluated by multiple consecutive cycle voltammetric experiments under a different range of potentials. Figure 7 left, shows 50 repetitive cyclic voltammetry experiments carried out in exactly the same conditions as the previous one, but after changing the potential range from -1.08 till 1.19 V to fully reduce the initial complex all the way to the $\text{Fe}^{\text{II}}_5^{2+}$ species. Figure 7 right also shows the current density plot obtained at 1.19 V vs. $i_{p,a}$ of the $[\text{Fe}^{\text{II}}\text{Fe}^{\text{III}}_4]^{6+}/[\text{Fe}^{\text{II}}_2\text{Fe}^{\text{III}}_3]^{5+}$ redox wave. As the number of cycles proceed, the catalytic intensity at 1.19 V increases due to the increasing amount of FeOx adsorbed at the GC electrode until it reaches a plateau due to the saturation of the surface. On the other hand, the intensity of the molecular $\text{Fe}_5^{\text{n+}}$ species waves decrease due to a decrease of the concentration of the double layer caused by the formation of FeOx. As can be seen in the Figure 7, the FeOx deposited at the electrode is conductive. The formation of nanoparticles can be observed with SEM (see Figure S10 in the SI) with an approximate diameter of about 40 nm.

Figure 7.

The conductivity of the material also enables us to observe the formation of other electroactive species growing at the double layer (see cathodic waves at -0.25 and 0.75 V in Figure 7 left). This suggests that the initial Fe_5^{n+} complex decomposes to other molecular species as indicated in Figure 4, before forming FeOx which finally ends up being adsorbed at the surface of the electrode.

2.5 Potentiostatic generation of FeOx

Potentiostatic experiments were carried out using a carbon rod or an ITO as a working electrodes as shown in the SI (See Figure S12, S14 and S17).

A CPE was performed with a GCrod as working electrode with 6.5 mL of a 0.2 mM (1.3 μmol) solution of Fe_5^{3+} and was carried out for 1 h at $E_{\text{app}} = 1.19$ V. During this time 1.05 C were passed together with the formation of 2.5 μmol of O_2 that account for 90 of Faradaic Efficiency (FE) (see Figure S12 and S13). Oxygen detection obtained through Clark electrode.

Potentiostatic experiments using ITO electrodes ($S = 2 \text{ cm}^2$) as working electrodes are shown in the SI (Figure S14 and S17). Same conditions previously described, 6.5 mL of a 0.2 mM (1.3 μmol) solution of Fe_5^{3+} were applied. One CPE was carried out for 1 h at $E_{\text{app}} = 1.42$ V. During this time 7.5 C (77 μmol of electrons/4 = 19.4 μmol of O_2) were obtained which corresponds to a TN = 14.9 assuming a 100% FE (calculated for comparison purposes; see Figure S14). After the bulk electrolysis the ITO electrode was placed in a clean electrolyte solution and showed the same activity as in the presence of the Fe_5^{3+} solution, demonstrating again that the water oxidation activity is due the formation of FeOx at the surface of the electrode (Figure S15 left). Further, a CV using a GC disk as working electrode, was carried out for the Fe_5^{3+} solution obtained after the bulk electrolysis and showed no molecular species present indicating that the whole solution is transformed to FeOx (see Figures S15 and S16). An additional bulk electrolysis was carried out at $E_{\text{app}} = 1.19$ V (Figure S17) under the same conditions as in the previous case using an ITO electrode ($S = 2 \text{ cm}^2$), yielded 1 C (10.2 μmol of electrons/4 = 2.5 μmol of O_2) which corresponds to a TN = 1.9 assuming a 100% faradaic efficiency. The CV of the solution after the CPE shows that a significant amount of the initial complex together with other waves associated with potential decompositions of the initial Fe_5^{3+} complex are still present (Figure S18 right). This implies that the initial complex has only been partially decomposed to FeOx and that this process is taking place slowly and in parallel to the electrocatalytic formation of O_2 by the adsorbed FeOx.

Discussion

The compact structure of the Fe_5^{3+} complex is a highly stable structural arrangement and thus constitutes a thermodynamic sink in the sense that all intermediate species generated from the reaction of bpp^- and Fe(II) can break and form new Fe-N bonds until they end up trapped in Fe_5^{3+} . This implies that bond formation and breaking acts as an automatic healing process that leads to the final Fe_5^{3+} complex. A similar type of phenomena has been described in supramolecular chemistry for the generation of macrocycles and cages based on other transition metals (Cook, Zheng and Stang, 2013). This large stability is also displayed by related tetradentate linear ligands with Fe and other first row transition metal complexes such as Mn that generate virtually identical structures (Kabata-pendias and Mukherjee, 2007). The large degree of stability is also manifested in the large energy value (18.9 kcal/mol) calculated that is required to coordinate an additional water molecule to one of the equatorial Fe center, changing its first coordination sphere from CN_5 to CN_6 . These pentanuclear complexes are very stable from a thermodynamic perspective but they also are highly labile due their high spin electronic configurations. Thus, while these complexes are stable in MeCN solution, they readily decompose in the presence of coordinating solvents such as water, where the latter competes for the first coordination sphere. This decomposition phenomenon involves the disruption of the whole complex leading to a structure crumbling effect that finally generates the $[\text{M}(\text{H}_2\text{O})_6]^{2+/3+}$ and the free ligand as has been reported for Mn_5^{3+} case. The Fe_5^{3+} complex is slightly more stable than its Mn analogue and can tolerate concentrations up to 10:1 MeCN:H₂O at low oxidation states. However, the stability of the complex is reduced in its high oxidation state species even in MeCN. While the $[\text{Fe}^{\text{II}}\text{Fe}^{\text{III}}_4]^{6+}$ decomposes completely in about 1 h, the $[\text{Fe}^{\text{III}}_5]^{7+}$ decomposes much faster and has not been isolated (Gouré *et al.*, 2016). Electrochemically, the $[\text{Fe}^{\text{II}}\text{Fe}^{\text{III}}_4]^{6+}$ species are not stable in a 10:1 MeCN:H₂O solution as ascertained by CV leading to the aquated species (Figure 4). Additionally, increasing the applied potential to the zone of predominance of the $[\text{Fe}^{\text{III}}_5]^{7+}$ species, lead to the formation of FeOx concomitant with the generation of a large electrocatalytic water oxidation current. The fact that the foot of the electrocatalytic current is found at a 150 mV lower potential than the foot of the $[\text{Fe}^{\text{III}}_5]^{7+}/[\text{Fe}^{\text{II}}\text{Fe}^{\text{III}}_4]^{6+}$ couple suggests that both the $[\text{Fe}^{\text{II}}\text{Fe}^{\text{III}}_4]^{6+}$ and the $[\text{Fe}^{\text{III}}_5]^{7+}$ might be responsible for the aquation of the Fe_5^{n+} species that lead to the formation of FeOx adsorbed at the electrode. Given the large stability of the Fe_5^{n+} structure, once a water adds to the first coordination sphere of an equatorial Fe center, the whole structure immediately crumbles giving rise to a large number of potential species as outlined in Figure 4. This view is also in agreement with the increased catalytic activity obtained upon increasing the H₂O concentration which shifts the equilibria to the right as shown in Figure 3. These molecular high oxidation state species generated at high potentials from the dismantling of

the Fe_5^{nt} structure could potentially behave as water oxidation catalysts. However, in the present case, given the large activity associated with FeOx, the activity of the resulting decomposed species is small if not active at all, as evidenced by CV experiments in clean electrolyte solutions.

All these experiments suggest the presence of a very delicate equilibrium between the $[\text{Fe}^{\text{II}}\text{Fe}^{\text{III}}_4]^{6+}$ and the $[\text{Fe}^{\text{III}}_5]^{7+}$ species and their aquated counterparts as proposed in Figure 4. An additional evidence of this delicate equilibrium is exemplified by the experiments carried in the presence of the triflic acid that completely suppresses catalysis. Further, the experiments carried out at different pHs suggest the local pH close to the electrode can reach pH values as low as 1, in experiments carried out in the absence of a buffer, for instance in a 10:1 MeCN:H₂O solvent. The low pH conditions could further help in the aquation of the Fe_5^{3+} complex and thus in the generation of FeOx.

An additional interesting point that also emerges from this work is how the nature of the FeO_x formed at the surfaces of the electrode (conductive vs. isolating; films vs. nanoparticles), is strongly dependent on the potential range used to generate it. Further, it is also striking to see the high activity of this FeOx adsorbed at the surface of the electrode that reaches current densities in the range of 3 mA/cm² at pH 7.

In this regard, the high activity of the FeOx could lead to a misinterpretation of the results if the working electrodes are not properly evaluated in clean electrolyte solutions, since only very small amounts of the initial molecular complex are needed to be transformed into highly active FeOx. Thus, in the hypothetical case that the stability of the complex in solutions after a bulk electrolysis experiment was checked, for instance by UV-vis, MS or DLS spectroscopy, it would appear as if the initial catalyst was intact as the initial concentration would remain practically the same.

Several main conclusions can be inferred from the present work. In the first place, the auxiliary ligands used in WOCs with transition metals should contain oxidatively robust ligands given the high redox potentials of this reaction. Therefore, ligands containing benzyl pyridyl groups will be easily oxidized as has been shown in many cases (Radaram *et al.*, 2011; Sander *et al.*, 2015; Wang, Sahoo and Lu, 2016). and thus they should not be used in their ligand framework. Secondly, special attention should be given at the stability first row transition metals in water given the high lability of the M-L bond in this solvent (Helm and Merbach, 2006). The aqua substitution will foster the formation of oxides adsorbed at the surface of the electrode. Finally, the fact that the water oxidation reaction generates four protons per oxygen molecule implies that a buffer should always be used to avoid ligand decoordination and oxide formation.

Limitation of the Study

No limitation of the study can be declared.

Resource Availability

Lead Contact: Further information requests should be directed to the Lead Contact, Antoni Llobet (*allobet@iciq.cat*).

Materials Availability: No new reagents were synthesized. There are no restrictions to the availability of chemicals.

Data and Code Availability: Crystallographic information for $[\text{Fe}^{\text{II}}_2\text{Fe}_3^{\text{III}}]^{5+}$ with CCDC number 1963878 is available at <https://www.ccdc.cam.ac.uk/>.

Methods

Detail about the experimental procedures can be found in the Supplemental Information.

Supplemental Information

Experimental details together with additional, analytic, spectroscopic and electrochemical data.

Acknowledgements.

Support from MINECO, FEDER and AGAUR are gratefully acknowledged through grants CTQ2016-80058-R, CTQ2015-73028-EXP, SEV 2013-0319, ENE2016-82025-REDT, CTQ2016-81923-REDC, and 2017-SGR-1631. D.M acknowledges funding from the Severo Ochoa (SEV-2016-0686) Excellence Program from IMDEA Nanociencia. XAS experiments were performed at the CLAEISS beamline at ALBA Synchrotron under proposal No. 20170913.

Author Contributions

A. L. conceived the idea of the project. P. P. performed the synthesis, characterization and electrochemical experiments. M. G.-S. assisted with the electrochemical experiments. D. M. performed the XAS experiments. All authors contributed to the design of experiments, analysis of the results and preparation of the manuscript.

Declaration of Interests

The authors declare no competing interests.

References

- Bao, X., Leng, J.-D., Meng, Z.-S., Lin, Z.-J., Tong, M.-L., Nihei, M., and Oshio, H. (2010). Tuning the Spin States of Two Apical Iron(II) Ions in the Trigonal-Bipyramidal $[\{\text{Fe}^{\text{II}}(\mu\text{-bpt})_3\}_2\text{Fe}^{\text{II}}_3(\mu_3\text{-O})]^{2+}$ Cations Through the Choice of Anions. *Chem. Eur. J.* *16*, 6169–6174.
- Berardi, S., Drouet, S., Francàs, L., Gimbert-Suriñach, C., Guttentag, M., Richmond, C., Stoll, T., and Llobet, A. (2014). Molecular artificial photosynthesis. *Chem. Soc. Rev.* *43*, 7501–7519.
- Blakemore, J. D., Crabtree, R. H., and Brudvig, G. W. (2015). Molecular catalysts for water oxidation. *Chem. Rev.* *115*, 12974–13005.
- Chen, G., Chen, L., Ng, S.-M., Man, W.-L., and Lau, T.-C. (2013). Chemical and Visible-Light-Driven Water Oxidation by Iron Complexes at pH 7–9: Evidence for Dual-Active Intermediates in Iron-Catalyzed Water Oxidation. *Angew. Chem. Int. Ed.* *52*, 1789–1791.
- Cook, T. R., Zheng, Y. R., and Stang, P. J. (2013). Metal–Organic Frameworks and Self-Assembled Supramolecular Coordination Complexes: Comparing and Contrasting the Design, Synthesis, and Functionality of Metal–Organic Materials. *Chem. Rev.* *113*, 734–777.
- Croce, R., and van Amerongen, H. (2014). Natural strategies for photosynthetic light harvesting. *Nat. Chem. Biol.* *10*, 492–501.
- Draksharapu, A., Li, Q., Logtenberg, H., Van den Berg, T. A., Meetsma, A., Killeen, J. S., Feringa, B. L., Hage, R., Roelfes, G., and Browne, W. R. (2012). Ligand exchange and spin state equilibria of $\text{Fe}^{\text{II}}(\text{N4Py})$ and related complexes in aqueous media. *Inorg. Chem.* *51*, 900–913.
- Ellis, W. C., McDaniel, N. D., Bernhard, S., and Collins, T. J. (2010). Fast water oxidation using iron. *J. Am. Chem. Soc.* *32*, 163–170.
- Folkman, S. J., Soriano-Lopez, J., Galá-Mascarós, J. R., and Finke, R. G. (2018). Electrochemically Driven Water-Oxidation Catalysis Beginning with Six Exemplary Cobalt Polyoxometalates: Is It Molecular, Homogeneous Catalysis or Electrode-Bound, Heterogeneous CoOx Catalysis? *J. Am. Chem. Soc.* *140*, 12040–1205.
- Garrido-Barros, P., Gimbert-Suriñach, C., Matheu, R., Sala, X., and Llobet, A. (2017). How to make an efficient and robust molecular catalyst for water oxidation. *Chem. Soc. Rev.* *46*, 6088–6098.
- Godwin, I., Rovetta, A., Lyons, M., and Coleman, J. (2018). Electrochemical water oxidation: The next five years. *Curr. Opin. Electrochem.* *7*, 31–35.
- Gouré, E., Gerey, B., Clémancey, M., Pécaut, J., Molton, F., Latour, J. M., Blondin, G., and Collomb, M. N. (2016). Intramolecular Electron Transfers Thwart Bistability in a Pentanuclear Iron Complex. *Inorg.*

Chem. 55, 9178–9186.

Grätzel, M. (1981). Artificial photosynthesis: water cleavage into hydrogen and oxygen by visible light. *Acc. Chem. Res.* 14, 376–384.

Guan, X., Chowdhury, F. A., Wang, Y., Pant, N., Vanka, S., Trudeau, M. L., Guo, L., Vayssieres, L., and Mi, Z. (2018). Making of an industry-friendly artificial photosynthesis device. *ACS Energy Lett.* 3, 2230–2231.

Helm, L., and Merbach, A. E. (2006). Inorganic and Bioinorganic Solvent Exchange Mechanisms. *Chem. Rev.* 105, 1923-1960.

Hoffert, W. A., Mock, M. T., Appel, A. M., and Yang, J. Y. (2013). Incorporation of Hydrogen-Bonding Functionalities into the Second Coordination Sphere of Iron-Based Water-Oxidation Catalysts. *Eur. J. Inorg. Chem.* 22-23, 3846-3857.

Hong, D., Mandal, S., Yamada, Y., Lee, Y. M., Nam, W., Llobet, A., and Fukuzumi, S. (2013). Water Oxidation Catalysis with Nonheme Iron Complexes under Acidic and Basic Conditions: Homogeneous or Heterogeneous? *Inorg. Chem.* 52, 9522–9531.

Kabata-pendias, A., and Mukherjee, A. B. (2007). Trace Elements From Soil to Human. (Ed., Springer).

Kaeffer, N., Morozan, A., Fize, J., Martinez, E, Guetaz, L., and Artero, V. (2016). The dark side of molecular catalysis: Diimine–Dioxime Cobalt Complexes Are Not the Actual Hydrogen Evolution Electrocatalyst in Acidic Aqueous Solutions. *ACS Catal.* 6, 3727-3737.

Keidel, A., Lopez, I., Staffa, J., Kuhlmann, U., Bozoglian, F., Gimbert-Surinach, C., Benet-Buchholz, J., Hildebrandt, P., and Llobet, A. (2017). Electrochemical and resonance Raman spectroscopic studies of water-oxidizing ruthenium terpyridyl-bipyridyl complexes. *ChemSusChem* 10, 551-561.

Kuzmin, A.; Chaboy, J. (2014). EXAFS and XANES analysis of oxides at the nanoscale. *IUCr* ,1, 571-589. DOI: 10.1107/s2052252514021101.

Le Formal, F., Pastor, E., Tilley, S. D., Mesa, C. A., Pendlebury, S. R., Grätzel, M., and Durrant, J. R. (2015). Rate law analysis of water oxidation on a Hematite surface. *J. Am. Chem. Soc.* 137, 6629-6637.

Lewis, N. S., and Nocera, D. G. (2006). Powering the planet: Chemical challenges in solar energy utilization. *Proc. Nat. Acad. Sci.* 103, 15729-15735.

Lewis, N. S., and Nocera, D. G. (2007). Correction for Lewis and Nocera, Powering the planet: Chemical challenges in solar energy utilization. *Proc. Nat. Acad. Sci.* 104, 20142-20142.

- Lewis, N. S. (2016). Research opportunities to advance solar energy utilization. *Science* *351*, 353–361.
- Liao, R. Z., Masaoka, S., and Siegbahn P. E. M. (2018). On the metal oxidation states for the O-O bond formation in the water oxidation catalyzed by a pentanuclear Iron complex. *ACS Catal.* *8*, 11671–11678.
- Llobet, A., and Meyer, F. (2011). Water oxidation in the context of the energy challenge: tailored transition-metal catalysts for oxygen-oxygen bond formation. *Angew. Chem. Int. Ed.* *50*, 30-33.
- Matheu, R., Ertem, M. Z., Benet-Buchholz, J., Coronado, E., Batista, V. S., Sala, X., and Llobet, A. (2015). Intramolecular Proton Transfer Boosts Water Oxidation Catalyzed by a Ru Complex. *J. Am. Chem. Soc.* *137*, 10786-10795.
- Matheu, R., Garrido-Barros, P., Gil-Sepulcre, M., Ertem, M. Z., Sala, X., Gimbert-Suriñach, C., and Llobet A. (2019). The development of molecular water oxidation catalysts. *Nat. Rev. Chem.* *3*, 331–341.
- Matheu, R., Ertem, Z. M., Gimbert-Suriñach, C., Sala, X., and Llobet, A. (2019). Seven coordinated molecular ruthenium-water oxidation catalysts: A coordination chemistry journey. *Chem. Rev.* *119*, 3453-3471.
- McCrary, C. C. L., Jung, S., Ferrer, I. M., Chatman, S. M., Peters, J. C., and Jaramillo, T. F. (2015). Benchmarking hydrogen evolving reaction and oxygen evolving reaction electrocatalysts for solar water splitting devices. *J. Am. Chem. Soc.* *137*, 4347–4357.
- McEvoy, J. P., and Brudvig, G. W. (2006). Water-splitting chemistry of photosystem II. *Chem. Rev.* *106*, 4455–4483.
- Nelson, N., and Ben-She, A. (2004). The complex architecture of oxygenic photosynthesis. *Nat. Rev. Mol. Cell. Biol.* *5*, 971–982.
- Nocera, D. G. (2017). Solar fuels and solar chemicals industry. *Acc. Chem. Res.* *50*, 616–619.
- Okamura, M., Kondo, M., Kuga, R., Kurashige, Y., Yanai, T., Hayami, S., Praneeth, V. K. K., Yoshida, M., Yoneda, K., Kawata, S., and Masaoka, S. (2016). A pentanuclear iron catalyst designed for water oxidation. *Nature* *530*, 465–468.
- Pattanayak, S., Chowdhury, D. R., Garai, B., Singh, K. K., Paul, A., Dhar, B. B., and Gupta, S. S. (2017). Electrochemical Formation of FeV(O) and Mechanism of Its Reaction with Water During O–O Bond Formation. *Chem. Eur. J.* *23*, 3414-3424.

- Radaram, B., Ivie, J., Singh, W. M., Grudzien, R. M., Reibenspies, J. H., Webster, C. E., and Zhao, X. (2011). Water Oxidation by Mononuclear Ruthenium Complexes with TPA-Based Ligands. *Inorg. Chem.* *50*, 10564-10571.
- Roger, I., Shipman, M. A., and Symes, M. D. (2017). Earth-abundant catalysts for electrochemical and photoelectrochemical water splitting. *Nat. Rev. Chem.* *1*, 301–313.
- Romain, S., Rich, J., Sens, C., Stoll, T., Benet-Buchholz, J., Llobet, A., Rodriguez, M., Romero, I., Clerac, R., Mathoniere, C., Duboc, C., Deronzier, A., and Collomb M. N. (2011). Multireversible Redox Processes in Pentanuclear Bis(Triple-Helical) Manganese Complexes Featuring an Oxo-Centered triangular $\{Mn^{II}_2Mn^{III}(\mu_3-O)\}^{5+}$ or $\{Mn^{II}Mn^{III}_2(\mu_3-O)\}^{6+}$ Core Wrapped by Two $\{Mn^{II}_2(bpp)_3\}^-$. *Inorg. Chem.* *50*, 8427–8436.
- Sala, X., Maji, S., Bofill, R., Garcia-Anton, J., Escriche, L., and Llobet, A. (2014). Molecular water oxidation mechanisms followed by transition metals: State of the art. *Acc. Chem. Res.* *47*, 504-516.
- Sander, A. C., Schober, A., Dechert, S., and Meyer, F. (2015). A Pyrazolate-Bridged Bis(pentadentate) Ligand and Its Dinuclear Ruthenium Complex. *Eur. J. Inorg. Chem.* 4348-4353.
- Sens, C., Rodríguez, M., Romero, I., Llobet, A., Parella, T., and Benet-Buchholz, J. (2003). Synthesis, Structure and Acid-base and Redox Properties of a Family of New Ru(II) Isomeric Complexes Containing the Trpy and the Dinucleating Hbpp Ligands. *Inorg. Chem.* *42*, 8385-8394.
- Smith, R. D., Prévot, M. S., Fagan, R. D., Zhang, Z., Sedach, P. A., Siu, M.K., Trudel, S., and Berlinguette, C. P. (2013). Photochemical route for accessing amorphous metal oxide materials for water oxidation catalysis. *Science* *340*, 60–63.
- Sreerama, S. G., and Pal, S. (2004). A triiron complex containing the carboxylate-free $\{Fe_3(\mu_3-O)\}^{7+}$ core and distorted pentagonal-bipyramidal metal centres. *Eur. J. Inorg. Chem.* *3*, 4718–4723.
- Tangwatanakul, W.; Sirisathitkul, C.; Limphirat, W.; Yimnirun, R. (2017). Synchrotron X-ray absorption of iron oxide (Fe₂O₃) nanoparticles: Effects of reagent concentration and sonication in co-precipitation synthesis. *Chinese Journal of Physics*, *55*, 845.
- Wang, J.-W., Sahoo, P., and Lu, T.-B. (2016). *ACS Catal.* *6*, 5062-5068.

Main figure titles and legends

Figure 1. Crystal structure of Fe_5^{5+} . Left, ball and stick drawing of the cationic part of $[\text{Fe}^{\text{II}}_2\text{Fe}_3^{\text{III}}]^{5+}$. The Fe centers and the oxygen atoms are represented as green and red spheres respectively. The two Fe(II) centers are situated in the equatorial plane of the bipyramid. The bpp^- ligand is represented with gray sticks. H atoms are not drawn for simplicity reasons. Top right, partial representation of the upper part of bipyramidal structure of the Fe_5^{5+} complex showing only 2 out of the 6 bpp^- ligands (for simplicity purposes) bridging axial and equatorial Fe centers. Bottom right, drawn structure of the bpp^- (L^-) ligand and its representation using arcs connected with N.

Figure 2. Electrochemical characterization in MeCN of Fe_5^{3+} . Cyclic voltammetry experiments for Fe_5^{3+} 0.2 mM dissolved in a 0.1 M TEAP MeCN solution ($V_i = V_f = -0.24$ V; $V_{C1} = -1.08$ V; $V_{C2} = 1.42$ V) black trace, and in a 10:1 MeCN:H₂O volume ratio ($V_i = V_f = -0.24$ V, $V_{C1} = -1.08$ V; $V_{C2} = 1.19$ V) red trace (background subtracted) at a scan rate of 10 mV/s. Labels indicate the oxidation state zones of predominance as a function of potential. The inset shows an enlargement of the 0.6-1.4 V zone. See also Tables S1-2 and Figure S4.

Figure 3. Electrochemical analysis at different amount of water. Left, black trace, CV of the third cycle for Fe_5^{3+} 0.2 mM dissolved in a 10:1 MeCN:H₂O solution ($V_i = V_f = -1.08$ V; $V_{C1} = 1.19$ V) at a scan rate of 10 mV/s. Red trace, CV of the GC working electrode obtained in the previous experiment immersed in a clean electrolyte solution. Gray trace, CV of a bare GC electrode under the same conditions. Inset, enlargement in the zone of the non-catalytic waves of the complex. Right, plot of current density at 1.19 V under different MeCN:H₂O ratios obtained in the CV of: a) black trace, after 2.5 cycles for a 0.2 mM Fe_5^{3+} solution with a GC electrode as WE at the previous conditions; b) red trace, after the previous 2.5 cycles the GC electrode obtained is immersed in a clean electrolyte solution ($V_i = V_f = 0.92$ V; $V_{C1} = 1.19$ V); c) gray trace, blank for a bare GC electrode. See also Figures S5A and S5B.

Figure 4. Scheme for the formation of FeOx from Fe_5^{3+} . Potential non-isolated intermediate decomposition species formed from the $\text{Fe}_5^{\text{n+}}$ complex towards the generation of free iron, $[\text{Fe}(\text{H}_2\text{O})_6]^{\text{n+}}$, and the subsequent formation of the catalytically active species FeOx detected at the surface of an electrode.

Figure 5. Stability analysis and formation of FeOx film. Left, 100 repetitive CV for Fe_5^{3+} 0.2 mM dissolved in 10:1 MeCN:H₂O ($V_i = V_f = -0.24$ V, $V_{C1} = -0.44$ V; $V_{C2} = 1.19$ V). Color code: black trace, first cycle; red trace, last cycle; gray traces, intermediate cycles displayed every 5 cycles. Right, blue trace, plot of the current density at 1.19 V as a function of CV cycles. Green trace, plot of $i_{p,a}$ of the $[\text{Fe}^{\text{II}}\text{Fe}^{\text{III}}_4]^{6+}/[\text{Fe}^{\text{II}}_2\text{Fe}^{\text{III}}_3]^{5+}$ redox wave as a function of CV cycles. See also Figures S8, S9, S11.

Figure 6. X-ray absorption spectroscopy of the FeOx electroactive species. Left, normalized Fe K-edge XANES of: a) the Fe_5^{3+} complex in a frozen mixture of 10:1 MeCN:H₂O (blue), b) the frozen solution obtained after bulk electrolysis of Fe_5^{3+} at and applied potential of 1.42 V for 30 min (green; see main text and SI for further experimental details); c) glassy carbon plate (used as a working electrode) obtained after 100 successive CV experiments carried out in the ranges of -0.44 to 1.19 V of 0.2 mM solution of the Fe_5^{3+} complex in a mixture of 10:1 MeCN:H₂O (brown); d) Fe_2O_3 powder (cyan). Right, Experimental Fourier transforms of k-weighted Fe EXAFS of the samples described in the left using the same color code. The red arrows indicate the main peaks associated with Fe_2O_3 . See also Table S3 and Figures S19-21.

Figure 7. Stability analysis and formation of FeOx active nanoparticles. Left, 50 repetitive CV for Fe_5^{3+} 0.2 mM dissolved in 10:1 MeCN:H₂O ($V_i = V_f = -0.24$ V, $V_{C1} = -1.08$ V; $V_{C2} = 1.19$ V). Color code: black trace, first scan; red trace, last scan; gray traces, intermediate cycles displayed every 5 cycles. Right, blue trace, plot of the current density at 1.19 V as a function of CV cycles. Green trace, plot of $i_{p,a}$ of the $[\text{Fe}^{\text{II}}\text{Fe}^{\text{III}}_4]^{6+}/[\text{Fe}^{\text{II}}_2\text{Fe}^{\text{III}}_3]^{5+}$ redox wave as a function of CV cycles. See also Figures S10 and S11.